Reaction modelling of hydrogen evolution on nickel phosphide catalysts: Density functional investigation

Syam Sadan[a], Ingeborg-Helene Svenum[b], Sander Ø. Hanslin[a], Jaakko Akola[a,c]

[a]*Department of Physics, Norwegian University of Science and Technology, NO-7491 Trondheim, Norway*
[b]*SINTEF Industry, P. O. Box 4760 Torgarden, NO-7465 Trondheim, Norway*
[c]*Computational Physics Laboratory, Tampere University, FI-33101 Tampere, Finland*

Abstract

Nickel phosphides (Ni_xP_y), particularly Ni_2P, are promising catalysts for the acidic hydrogen evolution reaction (HER). Using density functional theory (DFT), we model HER at the potential of zero charge (PZC), incorporating solvation effects via an explicit water cluster and implicit surrounding solvent. Comparing the Volmer, Tafel, and Heyrovsky steps under saturated hydrogen coverage on $Ni_2P(0001)$ terminations, we find that the Ni_3P_2 (pristine) surface termination prefers the Volmer-Volmer-Tafel (VVT) pathway with activation energy (E_a) of 0.57 eV. Conversely, the Ni_3P_2+4P (reconstructed) surface favors the Volmer-Heyrovsky (VH) pathway with E_a = 0.60 eV. For the pristine surface termination, the differential gas-phase hydrogen adsorption free energies (ΔG_{diff}) correlate with the Volmer and Tafel step reaction energies, and a linear Bell–Evans–Polanyi relationship for the calculated activation and reaction energies validates the usefulness of the ΔG_{diff} descriptor for the Volmer step under PZC conditions. Nickel atoms play a crucial role in H_2 production on both pristine and reconstructed surfaces, suggesting that modifications of the Ni sites can be used for catalyst design. Our findings highlight the importance of considering surface reconstruction and solvation effects on the HER catalytic performance.

1. Introduction

Global energy demand and greenhouse gas emissions have increased drastically with industrialization, a trend which is expected to continue [1–5]. Reliance on fossil fuels results in significant emissions, highlighting the need for a sustainable energy transition. Renewable energy sources offer solutions but are limited, for example, by seasonal and geographical factors [6–8]. Within this context, hydrogen production, especially through water electrolysis ("green" hydrogen), is recognized as a viable method for energy storage and transportation [9]. The high energy density of hydrogen and its zero emissions, when combined with renewable resources, support its role as an efficient energy carrier with broad access to renewable energy [6, 8, 10].

The primary step in producing hydrogen with renewable energy sources is water electrolysis powered by renewables [6]. However, green hydrogen production costs remain higher than traditional methods such as steam methane reforming and coal gasification [9]. A central step towards cost reduction is advancing efficient fuel cell technologies, essential for a "hydrogen transition." A major challenge in sustainable fuel cells is the high overpotential required for water electrolysis. Identifying abundant (cheap), stable, and effective electrocatalysts is crucial for enhancing hydrogen production [11].

While noble metals such as Au, Ag, Pt, and Pd are efficient, their scarcity and high-cost limit commercial viability [10]. Transition metal phosphides (TMPs) have emerged as potential catalysts due to their high electrical conductivity, abundance, and catalytic properties [10, 12–14]. Extensive computational and experimental research has been conducted on TMP hydrogen evolution reaction (HER) catalysts to understand the mechanisms behind their enhanced catalytic activity and sensitivity to doping [11, 13, 15–26]. Nickel phosphides (Ni_xP_y), particularly Ni_2P, are notable TMP catalysts for HER due to their stability and efficiency [19–31].

The catalytic activity of Ni_2P was initially predicted using density functional theory and later verified experimentally [19, 20, 32]. Subsequent studies extensively explored the thermodynamic and electronic aspects of HER via hydrogen adsorption on active sites of Ni_2P [14, 28, 33, 34]. Emphasis was given to Ni hollow sites, P top sites and Ni-P bridge sites as active sites, where the presence of phosphorus is identified to be vital [14, 19, 33, 35, 36]. Despite significant efforts to enhance the catalytic activity of Ni_2P through surface modifications such as doping and heterostructures [27, 37–41], computational analyses of HER transition states and activation energies remain limited.

Understanding the HER pathways and TS energies on Ni_2P surfaces is crucial for accurate reaction kinetics analysis. In an acidic environment, HER involves two key steps: the Volmer step and the Tafel/Heyrovsky step. The Volmer step involves H atom adsorption onto the catalyst surface, which is the primary step. The secondary step, Tafel or Heyrovsky, describes hydrogen molecule formation through recombining two adsorbed hydrogen atoms or an adsorbed hydrogen atom with a proton from the solvent, respectively.

HER studies on transition metals have given more emphasis for the route involving Volmer and Tafel steps [19, 36]. How-

ever, the evidence for the inferiority of the Heyrovsky step on Ni_2P compared to that of Tafel is limited, indicating the need for further investigation to determine the dominant HER pathway. Moreover, conclusions drawn from HER studies on Ni_2P based solely on gas-phase hydrogen adsorption studies, neglecting solvent effects, may be insufficient for accurate reaction kinetics representation [42]. Therefore, exploring alternative HER steps such as Heyrovsky along with Volmer and Tafel, considering solvent influence, and understanding TS energies on Ni_2P surfaces are critical for improving predictive models and catalyst design [42–48].

The present study employs DFT calculations along with a hybrid solvent (water) model, which describes the influence of interfacial water molecules and continuum bulk water on the reaction, to investigate HER pathways and energetics on Ni_2P surfaces. This approach takes the first steps towards realistically understanding reaction kinetics on Ni_2P and its (0001) terminations. The electrode systems are set under acidic conditions at a potential of zero charge (PZC). Effects on the reaction energetics due to electrode corrosion, variations in pH and applied potential, though critical, are beyond the immediate scope of this study [28, 42, 47, 49]. Our results demonstrate that Ni_2P surfaces display moderate ($\sim$ 0.6 eV) reaction barriers even under PZC, and that the favourable HER pathway depends on the surface termination (pristine / reconstructed). The role of Ni sites turns out crucial for the final H_2 production step (Tafel or Heyrovsky) providing opportunities for catalyst design.

The article is structured as follows: Section 2 covers methods, including electronic structure simulations and hydrogen adsorption studies. Section 3 presents results and discussion, starting with structural optimizations and analysis of hydrogen adsorption and HER. Subsections 3.3.1 and 3.3.2 compare the catalytic performance of pristine and reconstructed Ni_3P_2 surfaces. Finally, Section 4 summarizes the key findings.

2. Methods

2.1. Electronic structure simulations

The atomistic simulations were based on the density functional theory (DFT) of electronic structure as implemented in the Vienna Ab initio Simulation Package (VASP) [50–52]. The electron exchange and correlation (XC) interactions were described using the Perdew-Burke-Ernzerhof (PBE) functional within the general gradient approximations (GGA) [53]. The Kohn-Sham wavefunctions were represented in a plane wave basis set with an energy cut-off of 500 eV. The Brillouin zone was sampled using a 6×6×6 k-point mesh for bulk structure optimizations, while a 6×6×1 mesh was used for all other types of calculations (slab systems). To facilitate a smooth convergence of the calculations, the partial electron occupations in the vicinity of the Fermi level were approximated by a Gaussian smear with a k_BT energy of 0.1 (0.05) eV in the gas-phase (solvent) structural optimisations. The electronic degrees of freedom were relaxed until the eigenvalues change less than 10^{-8} eV in bulk structure optimizations and 10^{-6} eV in all other cases. The effective ionic core interacting with the valence electron density is approximated using the projector augmented wave method (PAW) [54]. The dispersion correction proposed by Grimme *et al.* [55] was applied for total energies and forces to test the effect on hydrogen adsorption, while the reaction simulations were performed without it.

The velocity-quenched molecular dynamics algorithm was used to relax the cell volume and shape of bulk structures and atomic positions. Unless specified otherwise, the conjugate gradient algorithm was employed for all other structure optimizations, and the absolute force value on any atom was set below 0.01 eV/. The projected wavefunctions are calculated in reciprocal space for bulk calculations and in real space for all other structures. Dipole corrections to the total energy and forces were applied systematically.

2×2 supercells of the catalyst surface with periodic boundary conditions were constructed from the converged bulk structure with 7 atomic layers and 20 vacuum, of which three bottom layers were constrained to the bulk positions. The reference slabs and their adsorption coverages were found to be non-magnetic through spin-polarised calculations. The choice and construction of structures follow the thermodynamic framework mentioned in the references [56–58].

2.2. Hydrogen adsorption

The thermodynamic feasibility of hydrogen adsorption on the candidate catalysts was analysed by changes in Gibbs Free energy for n hydrogen atoms,

$$\Delta G_{nH} = \Delta E_{ads} + \Delta F_{vib} - T\Delta S_H, \tag{1}$$

where ΔE_{ads} is the DFT (0 K) adsorption energy, ΔF_{vib} is the change in vibrational free energy and ΔS_H is the entropy change upon adsorption. Consistent with the literature [38, 59], the entropy contribution of adsorbed hydrogen TS_{nH} was neglected, and the entropic energy of an H_2 molecule was considered as $TS_{H_2} = 0.403$ eV, referring to the standard tables for gas-phase molecules [60].

The average Gibbs free energy $\Delta G(n) = \Delta G_{nH}/nH$ describes the thermodynamic feasibility of hydrogen adsorption on the catalyst relative to the pristine reference surface. The smallest $\Delta G(n)$ indicates the optimum adsorption configuration at a particular coverage. The average Gibbs free energy does not provide adequate information regarding the feasibility of adsorbing additional hydrogen atoms to the given coverage. Such information is obtained using the differential Gibbs free energy,

$$\Delta G_{diff}(n) = \Delta G_{nH} - \Delta G_{(n-1)H}, \tag{2}$$

which takes into account the configurational change between n and $n+1$ hydrogens and enables identification of the saturation coverage according to the Sabatier principle [34, 61, 62]. The most favourable hydrogen adsorption coverages are marked by the thermoneutrality condition $\Delta G_{diff}(n) = 0$. To mitigate potential uncertainties stemming from computational details, such as the selection of the XC functional, dispersion correction, and other parameters, a thermoneutral range of

−0.1 to 0.1 eV is adopted to analyse differential Gibbs free energy results. This approach aligns with the methodology outlined in the references [34, 62].

To include temperature effects, the vibrational energy $E_{vib}(T,\omega)$ and entropy due to vibrations $S_{vib}(T,\omega)$ are calculated at T = 298 K. The corresponding equations have been adapted from the reference [63], and the vibrational corrections used to obtain Gibbs Free energy are discussed in the Supplementary Information (Eqs. 6, 7 and Table 1), respectively. The data associated with the present work's hydrogen adsorption calculations is available [64]. The H_2O adsorption calculations are omitted since reference [19] reviewed the competitive adsorption between H_2O and H on Ni_2P surface and found that H adsorbs stronger than H_2O or OH.

2.3. Hydrogen evolution reaction

The acidic HER is marked by two H^+ ions from the water forming an H_2 molecule often mediated by a catalyst surface. The three steps of the acidic HER cycle on a catalyst are given by,

$$H^+ + * + e^- \longrightarrow H* \qquad \text{(Volmer)} \qquad (3)$$

$$H* + H^+ + e^- \longrightarrow H_2 + * \qquad \text{(Heyrovsky)} \qquad (4)$$

$$2H* \longrightarrow H_2 + 2* \qquad \text{(Tafel)} \qquad (5)$$

where '*' represents a vacant site on the catalyst surface. To simplify the solvent description, an Eigen cation ($H_9O_4^+$, four explicit water molecules and a proton) surrounded by an implicit solvent was employed for all aqueous interface calculations. In the Volmer step, the H^+ from Eigen cation adsorbs at a vacant site on the catalyst surface. Depending on the reaction energetics, the system produces H_2 molecules either via Heyrovsky or Tafel step. The HER steps are schematically depicted in Figure 1. It is important to note that although the chemical equations represent charged species, the study uses a neutral simulation cell (i.e., neutral species initially). Herein, the Eigen cation acquires spontaneously a positive charge while the associated electron delocalises in the electrode.

The reaction energy (E_r) and activation energy (E_a) are the final state (FS) and transition state (TS) energies relative to the initial state (IS), respectively. These energies indicate the feasibility of a reaction step or cycle. Following the works of [36, 42], two consecutive Volmer steps and a Tafel step (VVT) were used to describe the E_r and E_a of a complete Tafel cycle for H_2 production around the saturation coverage. A similar approach was taken by combining Volmer and Heyrovsky steps (VH) for a complete cycle of the Heyrovsky mechanism.

All Volmer steps commence from a suitable hydrogen coverage configuration as the IS with an Eigen cation, $H_9O_4^+$. After adsorbing a H^+ from the water cluster, the reaction step attains an FS retaining four H_2O molecules. This means that an additional hydrogen must be present in the IS of the second Volmer step (V2) of VVT (or Heyrovsky step of VH) compared to the FS of the first Volmer step (V1). This discrepancy results in much lower energy for the IS of V2 compared to V1. To address this, a "proton-correction" was applied to the relevant energy profiles, accounting for the artificial hydrogen addition in the IS of V2. This adjustment removes the artificial stability increase for V2 and accurately reflects the effects of surface-Eigen cation interactions. This energy profile modification, modelled as a proton transfer from bulk water to the water cluster to form an eigencation, ensures mass (proton)-balanced profiles and accurate relative energies for consecutive Volmer and Volmer-Heyrovsky steps. This approach also facilitates later discussions. The corresponding chemical equation representing "proton-correction" is given in (6).

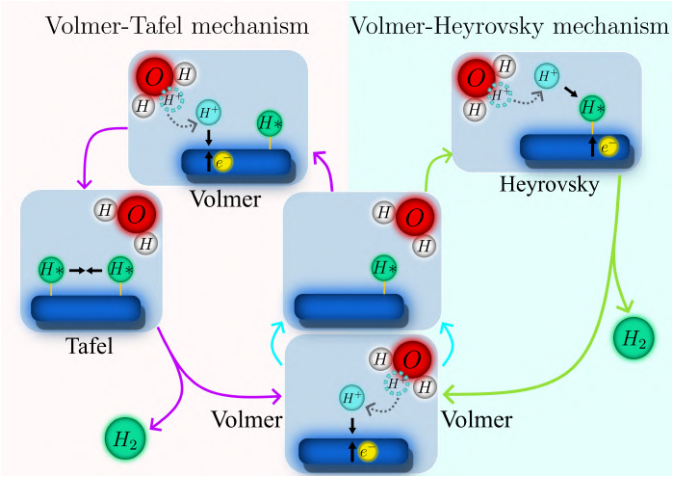

Figure 1: Schematics of the Volmer-Volmer-Tafel (VVT) and Volmer-Heyrovsky (VH) cycles for hydrogen evolution reaction on a catalyst surface. The figure was inspired by Ref. [65].

$$nH* + H_2O + H^+ \longrightarrow nH* + H_3O^+ \qquad (6)$$

In the VVT cycle, the catalyst surface proceeds from n to $n+2$ coverage via two successive Volmer steps that prepare the system in the desired coverage configuration for the Tafel step. After the Tafel step, a H_2 is formed from the two adsorbed H atoms. In the VH cycle, after the Volmer step, an H^+ from Eigen cation binds with an adsorbed hydrogen to form a desorbed H_2 molecule. This marks the Heyrovsky step of the cycle.

The VVT/VH cycles begin with a charged water cluster and conclude with an uncharged one. A proton transfer from the bulk water to the water cluster is required as a final step to achieve the charged state (IS) from the system's uncharged state (FS), marking the completion of the reaction cycle. Aligning the FS with that of the IS of the cycle ensures that the respective energies differ by ~0.01 eV only for all reaction cycles. Hence, the E_r values discussed in the following correspond to energies that do not include the final proton-correction.

The Eigen cation in conjugation with a description of the implicit solvent provides a practical approximation for the catalyst-solvent interaction. The implicit solvent formalism in VASPSol [66–68] was used to model the reactions. It is based on the joint DFT (jDFT) [69] where the electronic structure of the solute is modified by a classical density functional for liquid solvent. The total free energy functional is modified by adding Kohn-Sham, dielectric, and cavitation free energy contributions to represent a solute system in a continuum linear polarizable medium. All electrostatic interactions between the

solute and the solvent are included in the dielectric term, and all non-electrostatic interfacial interactions are approximated with the cavitation term. The ground state free energy of a solute-solvent system is obtained by minimizing the total free energy functional with respect to the electron density of the solute. For further details, refer to [66–68].

The Eigen cation ($H_9O_4^+$) was employed for reaction modelling, where H_3O^+ (hydronium) and $H_5O_2^+$ (Zundel) clusters are also possible. Hanslin et al. compared the energies of these ions with the Eigen cation and found convergence with increasing water cluster size [42]. It was also identified that an implicit solvent description is necessary to stabilise the protonated water clusters in reaction modelling [42].

A 2 × 2 surface with 5 (full) atomic layers was chosen for the candidate catalyst systems. The top two layers of the catalysts were relaxed, along with the adsorbed hydrogen atoms and the water cluster. The energy profiles of the HER cycles on catalyst surfaces were calculated using the climbing image-Nudged Elastic Band (CI-NEB) method [70–72]. The electronic and ionic optimizations converged below 10^{-6} eV and 0.05 eV/, respectively. The bulk relative permittivity of water ϵ_b was set to 78.4, and the Debye length λ_D to 3 , respectively. The remaining parameters are set to the default values in the VASPSol software [66–68]. The Fast Inertial Relaxation Engine (FIRE) [73] was used to optimise systems in solvent calculations. A detailed comparison of other force-based optimizers is provided in the reference [74]. The data from the HER calculations discussed in the work is available [75].

3. Results

3.1. Structure optimisations

The bulk structure of Ni_2P converged to a hexagonal lattice with lattice parameters a = b = 5.871 and c = 3.381 in a non-magnetic state. The Ni_2P bulk system has alternating layers of Ni_3P_2 and Ni_3P in the [0001] direction as illustrated in Figure 2a. The optimized structure agrees with the experimental lattice parameters a = b = 5.859 , c = 3.382 [76, 77], and is consistent with theoretical values in the literature [28, 56–58, 78].

The Ni_2P symmetric slabs of the Ni_3P and Ni_3P_2 surface terminations are illustrated in Figure 2b and the corresponding formation energy is plotted in Figure 2c. For the relevant range of phosphorus chemical potential (μ_P) in Ni_2P, the Ni_3P_2 termination is marginally more thermodynamically favourable than Ni_3P [27, 56, 58]. Based on this result, Ni_3P_2 was chosen as the candidate catalyst surface termination. Although Ni_3P is less favoured in comparison with Ni_3P_2, experiments suggest that both terminations are observed in Ni_2P [78–80]. The determination of lower (P-poor) and upper (P-rich) limits to μ_P is explained in Section SI1. For a detailed structural stability analysis of Ni_3P and other Ni_xP_y systems, we refer to [27, 28, 56, 58].

The thermodynamic stability of the Ni_3P_2 termination with additional P atoms, compared to the pristine (Ni_3P_2) termination, has been analyzed through formation energy calculations, as illustrated in Figure 3a. Among the enriched terminations, Ni_3P_2+5P is slightly more favourable towards the

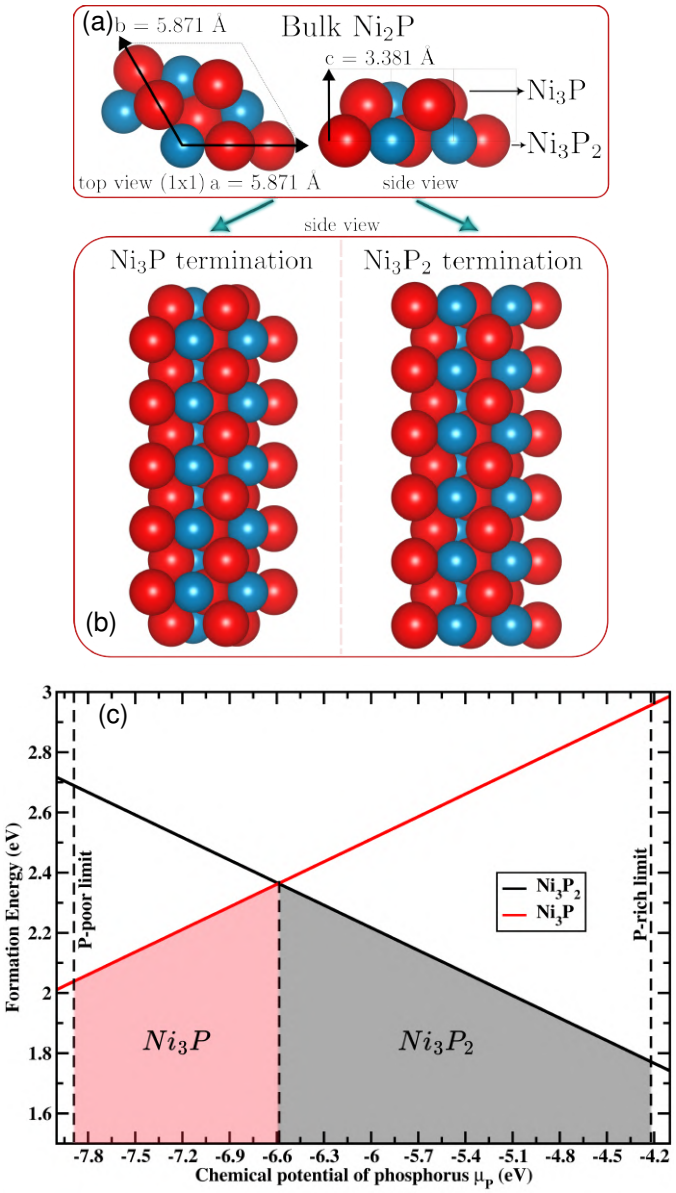

Figure 2: (a) Bulk structure of Ni_2P showing Ni_3P and Ni_3P_2 stacking with lattice parameters indicated. Red and blue colours represent Ni and P, respectively. (b) Ni_2P(0001) surface slabs of the Ni_3P and Ni_3P_2 terminations. (c) Formation energy for Ni_3P and Ni_3P_2 terminations in the phosphorus chemical potential range relevant for bulk Ni_2P formation.

end of the P-rich limit, while Ni_3P_2+4P is preferred within the middle-range of the μ_P limit. Motivated by the results given in Figures 2c and 3a, and the fact that both Ni_3P_2 (pristine) and Ni_3P_2+4P (reconstructed) terminations are experimentally observed [81, 82], both were considered as candidate surfaces for studying HER [57, 58]. Correspondingly, the P adatoms on the reconstructed surface termination occupy the Ni hollow sites, which are considered ideal for adsorption on the pristine surface [57, 58, 82]. Our results and the catalyst modelling are consistent with the literature [58, 83, 84]. An extensive outlook on Ni_2P surface terminations can be found in the literature [35, 56, 58].

The following hydrogen adsorption calculations were car-

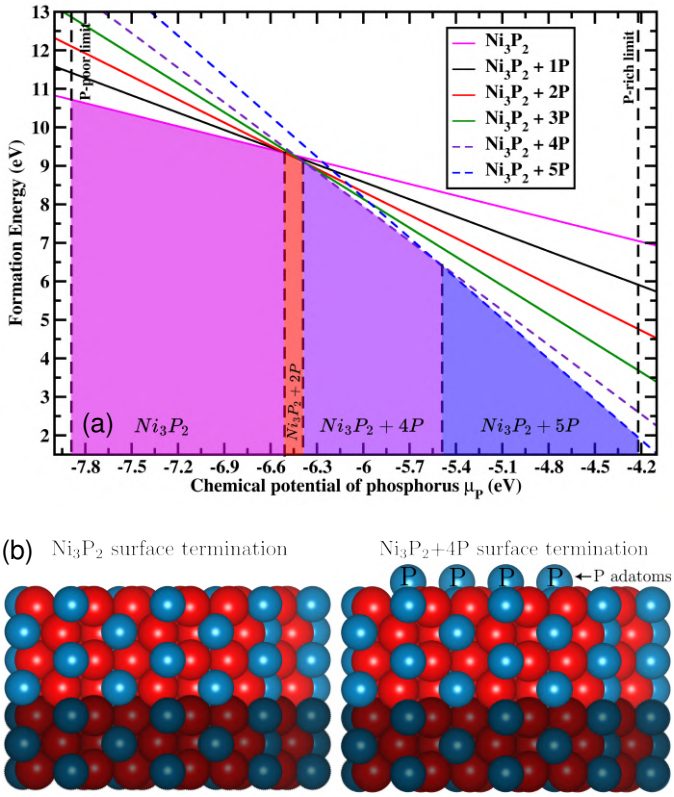

Figure 3: (a) Formation energy of the Ni_3P_2+XP (X = 1 to 5) terminated slabs over a chemical potential range relevant for bulk Ni_2P. The numbers of P atoms refer to the chosen 2×2 supercell in this work. (b) Side view of the $Ni_2P(0001)$ slabs with terminations Ni_3P_2 (left) and Ni_3P_2+4P (right). The three dark-shaded layers illustrate atoms with fixed bulk positions.

ried out on a 7-layered 2×2 surface of $Ni_2P(0001)$ asymmetric slab with Ni_3P_2 and Ni_3P_2+4P surface terminations (see Figure 3b).

3.2. Hydrogen adsorption

Table 1 displays the adsorption energies (ΔE_{ads}, eq. (1)) and Gibbs Free energies ($\Delta G(1)$, eq. (SI12)) of a single H atom adsorbed on Ni_3P_2 and Ni_3P_2+4P surfaces. The adsorption sites where H diffuses away to a more stable neighbouring site are excluded from the table. The hydrogen atom adsorbs the best on the Ni hollow site ($\Delta G(1)$ = -0.40 eV) on Ni_3P_2, and on the P adatom ($\Delta G(1)$ = 0.08 eV) on Ni_3P_2+4P. For pristine surface, the results indicate that only Ni hollow sites are preferred for increasing coverage. The positive $\Delta G(1)$ value of reconstructed Ni_3P_2+4P is due to the vibrational and entropic corrections (eq. (SI12)), while ΔE_{ads} is negative for the P adatom as well. Very similar adsorption free energy values (within 0.1 eV) have been found in the literature [14, 33, 62], although some works [36, 38] report weaker H adsorption relative to the present work. Table SI2 consolidates the gas-phase adsorption energy values from the literature.

Identifying the hydrogen saturation coverage on the pristine and reconstructed surface is crucial for setting a favourable condition for HER. Hence, a hydrogen coverage exploration on the catalyst surfaces is conducted based on differential

Table 1: Adsorption energy (ΔE_{ads}) and Gibbs Free energy ($\Delta G(1)$) of a single H atom adsorption without (with) dispersion corrections.

Adsorption site	Ni_3P_2	
	ΔE_{ads}(eV)	$\Delta G(1)$(eV)
Ni hollow	-0.62 (-0.68)	-0.40 (-0.46)
P top	0.10	0.36
Ni-P bridge	-0.02 (-0.12)	0.22 (0.12)
Adsorption site	Ni_3P_2+4P	
	ΔE_{ads}(eV)	$\Delta G(1)$(eV)
P top	0.19	0.44
Ni-P bridge	0.29	0.52
Ni top	0.00	0.21
adatom P	-0.18 (-0.25)	0.08 (0.05)

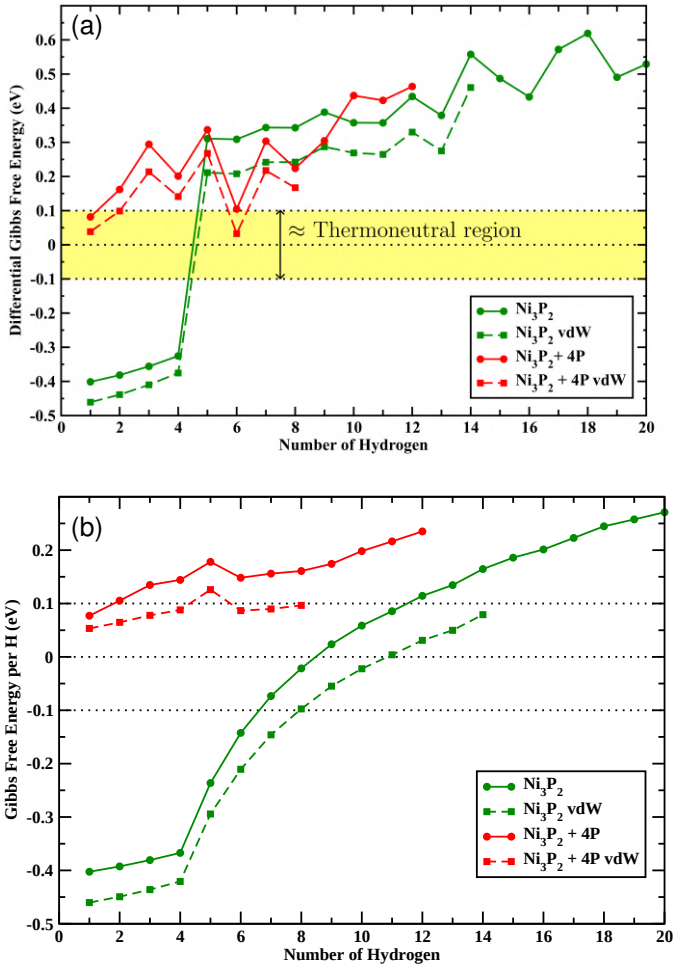

Figure 4: (a) Differential Gibbs Free energy (eq. (2)) and (b) average Gibbs free energy as a function of hydrogen coverage on the Ni_3P_2 (green) and Ni_3P_2+4P (red) surface terminations. The dashed (solid) curves represent results with (without) dispersion correction.

Gibbs Free energy ($\Delta G_{diff}(n)$) analysis. Figure 4a shows $\Delta G_{diff}(n)$ (eq. 2) for gas-phase hydrogen adsorption on Ni_3P_2 and Ni_3P_2+4P surfaces for variable coverage. $\Delta G_{diff}(n)$ denotes the cost or gain of adsorbing additional hydrogen from the preceding coverage configuration. A full-blown adsorption coverage study for higher coverages with all possible adsorp-

tion sites becomes a rapidly increasing combinatorial problem. Hence, the initial (unrelaxed) adsorption site configurations were constructed based on the site-specific information from the previous coverages. Figure 4b depicts $\Delta G(n)$ at various coverages. Considering possible computational inaccuracies, a thermoneutral region is defined between -0.1 to 0.1 eV to analyze the $\Delta G_{diff}(n)$ data following Refs. [34, 62].

Also, the relevance of the dispersion interaction in hydrogen adsorption is reported in Figure 4 for both surface types. The presented data with dispersion corrections extend only up to 14H and 8H on the pristine and reconstructed surfaces, respectively, since the uncorrected data showed consistently increasing endothermicity for higher coverages. The inclusion of the dispersion interaction results in slightly stronger hydrogen adsorption, which is also reflected in the differential Gibbs free energy as a small shift downwards. We considered this effect so small that we did not include dispersion corrections in the following reaction simulations.

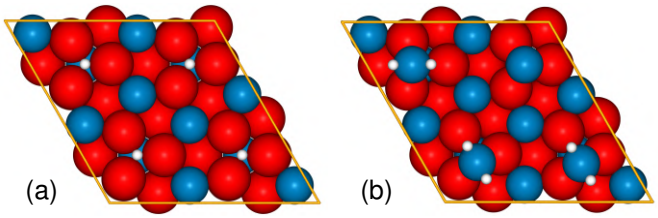

Figure 5: Saturated number of hydrogens adsorbed on (a) Ni_3P_2(4H) and (b) Ni_3P_2+4P(6H) surfaces with 2×2 unit cell.

As indicated by $\Delta G_{diff}(n)$, the 2×2 unit cell Ni_3P_2 surface termination saturates at four H atoms (nH = 4), each adsorbed at a hollow site. The adsorption is exothermic until all four hollow sites are covered (see Figure 5a), followed by a stepwise increase, and the larger coverages are increasingly endothermic. Consistent with the single H adsorption results, the Ni-P bridge sites become preferred ($\Delta G_{diff}(5)$ = 0.31 (0.21) eV) [19] after all hollow sites are filled. Such combinations of hollow and Ni-P bridge sites are the preferred adsorption configurations for up to 10 H atoms. A combination of Ni-Ni and Ni-P bridge sites with the hollow sites filled ($\Delta G_{diff}(10)$ = 0.37 (0.27) eV) emerged as the best hydrogen adsorption motif for 10 and higher numbers of H atoms on the pristine surface. The emergence of the Ni-Ni bridge as a preferred (and locally stable) adsorption site was only revealed through a coverage-exploratory study for larger numbers of H atoms. However, exploring coverages on supercells is a significant challenge, necessitating a faster method for identifying active sites and adsorption energies, as demonstrated by Ref. [85].

The preferred adsorption sites on the Ni_3P_2+4P surface termination consist of P adatoms covalently bonded to two or three H atoms (PH_2, PH_3), except for the cases of 1, 3, and 7 H atoms. For 3H and 7H, a PH_1 unit is preferred over a PH_3 in combination with the PH_2 unit(s). Pertaining to HER, coverages 1, 2, and 6 align with the thermoneutral region, amongst which 6 H (see Figure 5b) exhibits the most favourable adsorption. Identifying 6H as the best coverage once again demonstrates the necessity of conducting coverage-exploratory studies to find the optimal coverage for reaction simulations.

3.3. Hydrogen evolution reaction

The investigation of thermoneutral adsorption on the candidate catalysts suggests that the coverages of 4, 5, and 6 H atoms on the pristine surface and 6, 7, and 8 H atoms on the reconstructed surface are suitable for HER. Since alternative pathways will be explored in the following, we distinguish different configurations of the same coverage with Roman numerals in parenthesis adjacent to the coverage, e.g. nH(I), nH(II), etc. The following subsections provide a detailed discussion of E_a and E_r (consolidated in Table 2) of VVT and VH cycles on both pristine and reconstructed surfaces. For clarity, the VVT and VH pathways on the pristine surface will be denoted as PX_{VVT} and PX_{VH}, respectively, where "X" represents the specific pathway number (e.g., $P1_{VVT}$, $P2_{VH}$). Correspondingly, pathways on the reconstructed surface will be denoted as RX_{VVT} and RX_{VH}. Within each VVT pathway on the pristine surface (PX_{VVT}), the consecutive Volmer steps are denoted as PXV1 and PXV2 in chronological order. These steps are represented as RXV1 and RXV2 for the reconstructed surface. Similarly, the Volmer steps are labelled as PXV and RXV for the VH pathways. Finally, Tafel and Heyrovsky steps will be referred to as PXT / RXT and PXH / RXH for the pristine/reconstructed surfaces.

Additionally, proton-corrections were applied consistently to adjust the energy of the Volmer final states in all discussed pathways, accounting for the transfer of an additional proton from the bulk of water to the neutral water cluster (H_8O_4) in order to form an Eigen cation ($H_9O_4^+$) again. It should be noted that the final state energies of the pathways were not proton-corrected, as this correction straightforwardly sets their final energy close to zero. For further details, refer to section 2.3.

3.3.1. Pristine surface (Ni_3P_2)

Two energy profiles over various HER intermediates on the pristine surface are illustrated in Figure 6. The E_r and E_a (Table 2) reveal that the VVT cycle involving 3H(0), 4H(0), and 5H(0) coverages is the preferred pathway, denoted as $P1_{VVT}$ (Figure 6a). The E_a and E_r of the VVT cycle are 0.57 eV and 0.56 eV, respectively. Figure 7 visually represents the $P1_{VVT}$ cycle. The top view of relevant hydrogen coverage configurations involved in the cycle is depicted in Figure 5a, and Figures SI1a and SI1d. The consecutive Volmer steps proceed from 3H(0) to 5H(0) coverage going through 4H(0). The Tafel step (P1T) to form H_2 starts with 5H(0), where 4 H atoms are at the hollow site and one at a Ni-P bridge site. The Ni-P bridge hydrogen shares a Ni atom with one of the hollow site hydrogen (Figure SI1d). P1T results in the formation of H_2 on top of the Ni atom, and H_2 desorbs from the surface. The individual Volmer and Tafel energies (without proton-corrections) are summarized in Table SI3.

At one step higher H coverage, the energy profile of an alternative Tafel step P2T where the system goes from 6H(II) to 4H(I) + H_2 (Figure SI6b) is very close to that of P1T. Despite different numbers of H, the similarity between P1T and P2T can

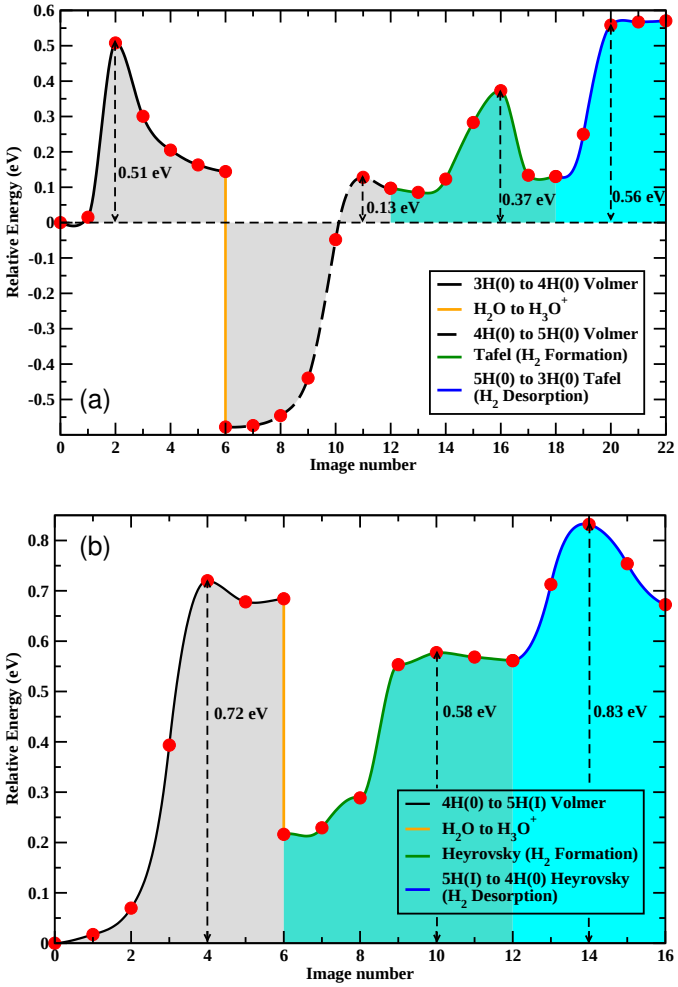

Figure 6: The energy profile of HER pathways on Ni_3P_2 surface termination. (a) Two consecutive Volmer steps from 3H(0) to 5H(0), and a Tafel step from 5H(0) to 3H(0) coverage corresponding to $P1_{VVT}$. (b) A Volmer step from 4H(0) to 5H(I), and a Heyrovsky step from 5H(I) to 4H(0) coverage corresponding to $P4_{VH}$.

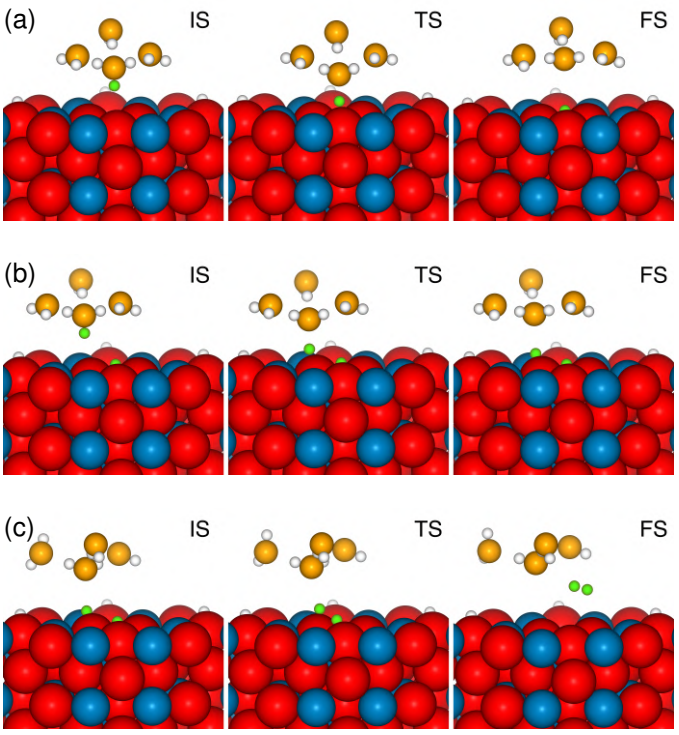

Figure 7: Volmer-Volmer-Tafel reaction pathway $P1_{VVT}$ on Ni_3P_2 via surface H coverages (a) 3 to 4, (b) 4 to 5 and (c) 5 to 3.

Table 2: Activation (E_a) and reaction (E_r) energy of reaction pathways. $PX_{VVT/VH}$ and $RX_{VVT/VH}$ represent Volmer-Volmer-Tafel/Volmer-Heyrovsky pathways of HER on pristine and reconstructed surfaces, respectively.

Pathway	Surface coverage transition	E_a (eV)	E_r (eV)
$P1_{VVT}$	3H(0)→4H(0)→5H(0)→3H(0)	**0.56**	**0.57**
$P2_{VVT}$	4H(0)→5H(I)→6H(II)→4H(I)	1.22	1.20
$P3_{VVT}$	4H(0)→5H(I)→6H(I)→4H(0)	0.95	0.68
$P4_{VH}$	4H(0)→5H(I)→4H(0)	0.83	0.67
$P5_{VH}$	4H(0)→5H(0)→4H(0)	0.82	0.74
$R6_{VVT}$	6H(0)→7H(0)→8H(0)→6H(0)	1.14	0.03
$R7_{VH}$	6H(0)→7H(I)→6H(0)	**0.60**	**-0.02**
$R8_{VH}$	6H(0)→7H(0)→6H(0)	0.93	0.06

be attributed to the correspondence in sites and atoms involved in the mechanism. The two mechanisms differ in energies by less than 0.05 eV.

Considering the Tafel energies solely (Table SI3), the most feasible pathway is from 6H(I) to 4H(0) + H_2 (P3T), see Figure SI6b. The E_a for H_2 formation in the P1T and P2T steps differ from that of P3T. The participation of a Ni hollow site H atom to form H_2 in P1T leads to an $E_a \approx 0.42$ eV higher than that for the Ni-P bridge site in P3T. Hence, the H_2 formation mediated by a Ni atom is affected by the adsorption sites of participating hydrogens. Therefore, the order of feasibility for the Tafel steps is P3T > P2T > P1T (Table SI3). As a whole, the VVT cycle E_r and E_a (with proton-corrections) suggest that the $P2_{VVT}$ pathway is undesired compared to $P1_{VVT}$ and $P3_{VVT}$. The order of preferential pathways for the VVT cycle is $P1_{VVT} > P3_{VVT} > P2_{VVT}$, see Table 2.

A comparison between the alternative pathways (see Table SI3) indicates that the Volmer steps and corresponding proton-corrections significantly influence the E_a and E_r of the cycles. Hence, modifications in the system that benefit Volmer steps should be considered when designing better HER catalysts. Since the gas phase differential adsorption energy $\Delta G_{diff}(n)$ correlates with the Volmer reaction energy (proton-corrected) over explored coverages, the relevant systems for reaction simulations can be screened based $\Delta G_{diff}(n)$ (Figure 8a), as suggested by Nørskov et al. [59]. Similar screening can be made for Tafel reaction studies by leveraging the correlation of gas phase differential adsorption energies (in steps of 2 hydrogens) with Tafel E_r shown in Figure 8b.

Among the two VH pathways examined, one progresses from 4H(0) to 5H(I) coverage and then returns to 4H(0) ($P4_{VH}$), while the other extends from 4H(0) to 5H(0) and then reverts to 4H(0) ($P5_{VH}$). The energy profile of $P4_{VH}$ ($P5_{VH}$) across the reaction intermediates is displayed in Figure 6b (Figure SI6d). The Figure SI3 provides a visual aid to enhance comprehension

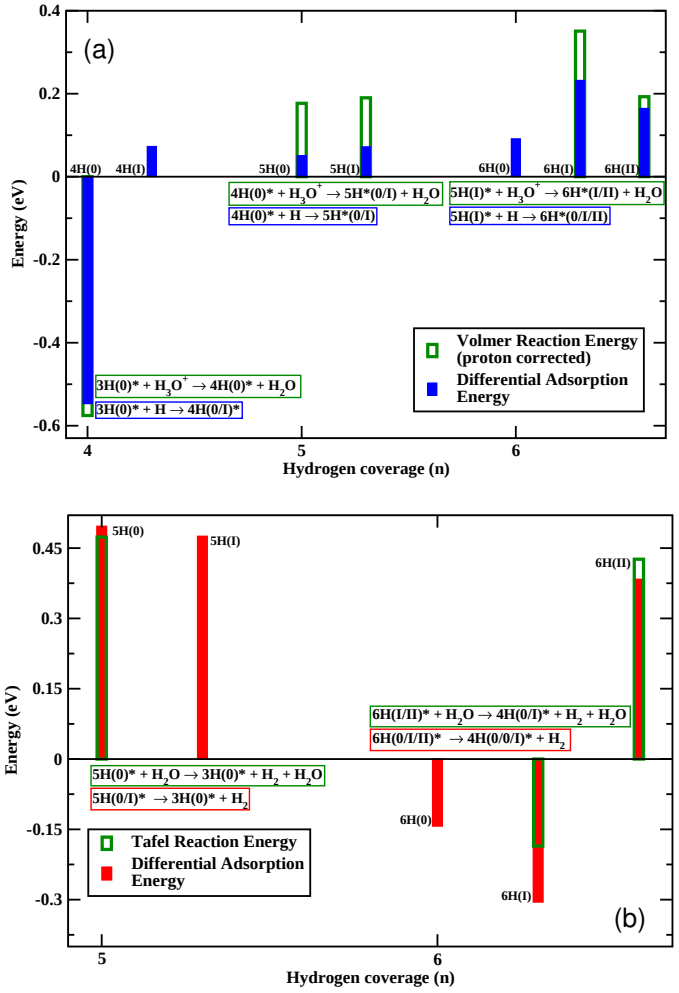

Figure 8: Comparison of (a) proton-corrected Volmer reaction energies with differential hydrogen adsorption energies in consecutive steps and (b) Tafel reaction energies with hydrogen adsorption energies in steps of two hydrogens as a function of coverage. Hydrogen coverage (n) is a positive integer value.

of the $P4_{VH}$ pathway. $P4_{VH}$ and $P5_{VH}$ exhibit similar VH energy profiles across the reaction intermediates, with the overall E_a/E_r of 0.83/0.67 eV and 0.82/0.74 eV, respectively. Both pathways exhibit similar barriers but slightly different E_r which differ by ≈ 0.1 eV (Table SI3), suggesting that the P4H is a slightly more preferred Heyrovsky step.

In $P4_{VH}$ and $P5_{VH}$, 4H(0) is the initial and final coverage, with 4 H atoms covering all Ni hollow sites (Figure 5a). The intermediate coverages 5H(0) and 5H(I) of the VH cycle have the fifth H adsorbed on a Ni-P bridge site, see Figures SI1d and SI1e, respectively. In preparation for H_2 formation, H adsorbed at the Ni-P bridge site ascends to the Ni top site before combining with H^+ from the solvent. The energy plateau observed towards the end of H_2 formation and the following uphill and barrier before desorption (Figure 6b) reflects the fact that H_2 prefers adsorption on the Ni top site compared to desorption. In both VVT and VH pathways, the Ni atom directly plays a substantial role in mediating the H_2 production.

The similarity in the Volmer steps of $P4_{VH}$ and $P5_{VH}$ (see Table SI3, Figures 6b , SI6d) is associated with the (bridge) adsorption sites in 5H(I) and 5H(0). As in the VVT pathways, the proton-corrected Volmer step was crucial in comprehending the overall energetics of the VH cycles and their feasibility. The bare Volmer reaction energetics are consistently higher than the bare Tafel and Heyrovsky steps (see Table SI3), and the proton-corrections improved the VVT/VH pathways.

Comparing the E_r and E_a of all HER pathways on the pristine surface, the reaction prefers $P1_{VVT}$ > $P4_{VH}/P5_{VH}$ > $P3_{VVT}$ > $P2_{VVT}$. The VVT pathways are not consistently better than VH, underscoring the significance of VH pathway studies in such systems. On the other hand, individual Tafel steps are energetically similar to or better than Heyrovsky steps.

3.3.2. *Reconstructed surface (Ni_3P_2+4P)*

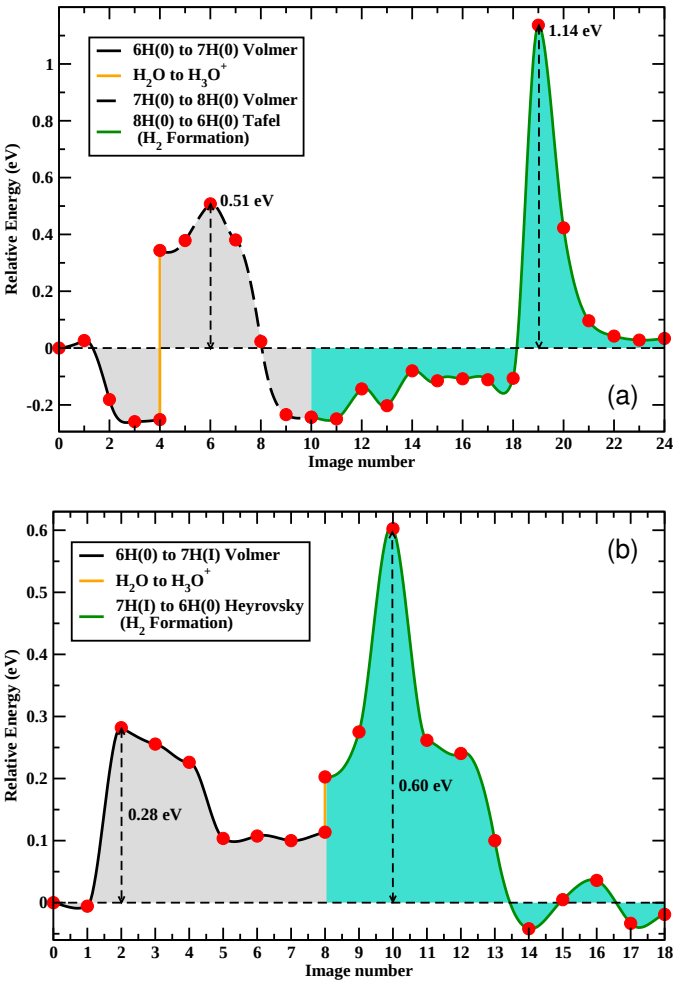

Figure 9: Energy profiles of HER pathways on Ni_3P_2+4P surface termination. (a) Two consecutive Volmer steps from 6H(0) to 8H(0) coverage, and a Tafel step from 8H(0) to 6H(0) corresponding to $R6_{VVT}$. (b) A Volmer step from 6H(0) to 7H(I) coverage, and a Heyrovsky step from 7H(I) to 6H(0) corresponding to $R7_{VH}$.

Similarly, as above, the VVT and VH pathways have been investigated on the reconstructed surface, and the energy profiles of two complete cycles are represented in Figure 9. The VVT pathway with 6H(0), 7H(0), and 8H(0) coverages ($R6_{VVT}$)

resulted in a high E_a (1.14 eV) whereas the E_r became low (0.03 eV). The reaction visualisation is provided in Figure SI4.

The two consecutive Volmer steps, R6V1 and R6V2, are both exothermic, helping to maintain a low E_r despite the positive proton-correction in between. The small fluctuations appearing after the second Volmer step are due to the diffusion of two H atoms on a P adatom to the pristine layer Ni top site. The Tafel energetics suggest that the orientation change/diffusion on the reconstructed surface is allowed with a negligible barrier. After the surface diffusion, the Ni atom mediates the H_2 formation. As observed on the pristine surface, the H_2 molecule prefers to adsorb on top of the Ni atom before desorption with a substantial energy barrier; see Image number 19 of Figure 9a.

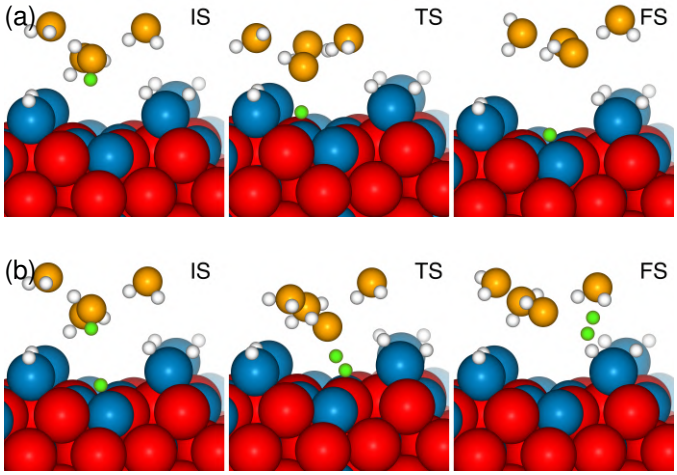

Figure 10: Volmer-Heyrovsky pathway R7 on Ni_3P_2+4P via surface hydrogen coverages (a) 6 to 7 and (b) 7 to 6.

Contrary to the pristine surface, proton-corrections led to a positive shift in the energy profile. Hence, they are not trivial and must be distinguished between the surfaces. The upward shift in the case of the reconstructed surface is due to the positive partial charge on the hydronium ion cluster and adatom phosphorus, which lie very close to each other, resulting in an unfavourable electrostatic situation. On the same grounds, the pristine surface accumulates electron density, resulting in a downward shift after proton-corrections.

Two alternative pathways, $R7_{VH}$ and $R8_{VH}$, are considered for the VH cycle on the reconstructed surface. The two pathways differ with respect to the 7H configuration. The top view of both 7H(0) ($R8_{VH}$) and 7H(I) ($R7_{VH}$) coverages are given in figures SI2b and SI2c, respectively. The energy profile and visualisations of the VH pathway $R7_{VH}$ are shown in figures 9b and 10, respectively. The motivation for investigating the $R7_{VH}$ pathway with a similar (0.05 eV difference) energy configuration 7H(I) arises from the fact that Ni atoms mediate H_2 formation, and the adatom-to-pristine-layer diffusion appears very feasible, as observed for the Tafel step from 8H(0) to 6H(0). Consistent with the pristine surface calculations, the seventh H atom at the Ni-P bridge site diffuses over the Ni top site and forms H_2 with the proton from the water cluster, resulting in an E_a/E_r of 0.60/-0.02 eV.

The second VH pathway, $R8_{VH}$, involves only lowest-energy configurations 6H(0) and 7H(0), as evidenced by the calculated Gibbs's free energy (Figure 4). The energy profile for $R8_{VH}$ is given in Figure SI6c. The added H atom in 7H(0) is adsorbed to the adatom phosphorus. Although the Volmer step is exothermic in the 7H(0) case, the VH cycle E_a is 0.3 eV higher than that of the 7H(I) case. The proton-correction is much more significant in $R7_{VH}$ than in the $R8_{VH}$, which is consistent with the electrostatic interaction of the water cluster and the adatoms.

Comparing the barrier heights in figures 9b and SI6c, the pathway $R7_{VH}$ is energetically more feasible than $R8_{VH}$ for the VH cycle. From Table SI3, the Heyrovsky mechanism appears to be favourable for H_2 production compared to Tafel, irrespective of the pathway. Hence, the order of preferential reaction cycles on the reconstructed surface is $R7_{VH} > R8_{VH} > R6_{VVT}$.

4. Discussion and conclusions

The catalytic activity of $Ni_2P(0001)$ surface terminations for acidic HER was investigated using DFT calculations. To understand the HER activity, potential terminations and reconstructions along the [0001] direction must be considered. Based on empirical and stability arguments, the present study focuses on Ni_3P_2 (pristine) and its Ni_3P_2+4P reconstruction, despite other viable terminations (Ni_3P) and phosphorus reconstructions.

Exploring critical hydrogen coverages is an essential starting point for HER investigations. The key coverages (based on ΔG_{diff}) are 3H(0), 4H(0), and 5H(0) on the pristine 2×2 surface, and 6H(0), 7H(0), and 8H(0) on the reconstructed surface. The pristine surface transitions from exothermic to endothermic adsorption between 4H(0) and 5H(0) as Ni hollow sites fill. 6H(0) with three PH_2 units is thermoneutral on the reconstructed surface. The subsequent HER simulations simulations (with solvent) show that the Volmer mechanism is crucial in determining the preferred cycle for both surface terminations. The eigencation-surface interaction has a non-trivial influence on the reaction energetics, depending on the termination and H coverage. The gas-phase adsorption energy correlates with the proton-corrected Volmer E_r on the pristine surface, which aids in screening potential Ni_2P-related HER catalysts.

For the Ni_3P_2 surface termination, the VVT cycle ($P1_{VVT}$ pathway) is more feasible than the VH cycle. In $P1_{VVT}$, surface coverage varies between 3H(0), 4H(0), and 5H(0), and the corresponding overall E_a and and E_r are 0.57 eV and 0.56 eV, respectively. The VVT pathways indicate that the strongly adsorbed H atoms (Ni hollow sites) can participate in H_2 formation with an associated energy cost. Tailoring catalysts via voltage and/or doping can enhance the role of such sites for HER.

The reconstructed Ni_3P_2+4P prefers the VH ($R7_{VH}$) mechanism for HER. The H coverage varies between 6H(0) and 7H(I), and the corresponding E_a and E_r are 0.60 eV and -0.02 eV, respectively. The Heyrovsky mechanism outperforms Tafel regardless of the pathway. The Tafel mechanism (pathway $R6_{VVT}$) suggests that the orientation change or diffusion onto the pristine-type second layer is feasible. Hence, electrochemi-

cal modifications on the second layer (Ni) can enhance H_2 production here as well by facilitating surface H atom diffusion.

Finally, the reaction simulations were conducted at PZC without applied voltage. We anticipate that applying voltage and/or doping will affect surface stability, including potential electrode corrosion, and consequently influence reaction energetics and mechanisms, such as transition states, as demonstrated for MoS_2 [42]. Such advanced catalysis modelling combining both voltage and solvent effects provides a more realistic and improved understanding of the reaction pathways and energetics.

Acknowledgements

The simulations were carried out using the supercomputing resources provided by Sigma2 - the National Infrastructure for High-Performance Computing and Data Storage in Norway, project No. NN9497K. We thank Prof. Hannes Jónsson for discussions.

References

[1] Meisam Mahdavi and David Vera. "Importance of renewable energy sources and agricultural biomass in providing primary energy demand for Morocco". In: *International Journal of Hydrogen Energy* (2023), pp. 34575–34598.

[2] Fengsheng Chien, Lihua Huang, and Wei Zhao. "The influence of sustainable energy demands on energy efficiency: Evidence from China". In: *Journal of Innovation & Knowledge* 8.1 (2023), p. 100298.

[3] Ch Mohan Sai Kumar et al. "Solar energy: A promising renewable source for meeting energy demand in Indian agriculture applications". In: *Sustainable Energy Technologies and Assessments* 55 (2023), p. 102905.

[4] Oguz Ozan Yolcan. "World energy outlook and state of renewable energy: 10-Year evaluation". In: *Innovation and Green Development* 2.4 (2023), p. 100070.

[5] Qiang Wang, Ting Yang, and Rongrong Li. "Does income inequality reshape the environmental Kuznets curve (EKC) hypothesis? A nonlinear panel data analysis". In: *Environmental Research* 216 (2023), p. 114575.

[6] VM Maestre, Alfredo Ortiz, and Inmaculada Ortiz. "Challenges and prospects of renewable hydrogen-based strategies for full decarbonization of stationary power applications". In: *Renewable and Sustainable Energy Reviews* 152 (2021), p. 111628.

[7] Michael Child et al. "Sustainability guardrails for energy scenarios of the global energy transition". In: *Renewable and Sustainable Energy Reviews* 91 (2018), pp. 321–334.

[8] RJ Lowe and P Drummond. "Solar, wind and logistic substitution in global energy supply to 2050–Barriers and implications". In: *Renewable and Sustainable Energy Reviews* 153 (2022), p. 111720.

[9] VA Panchenko et al. "Prospects for the production of green hydrogen: Review of countries with high potential". In: *International Journal of Hydrogen Energy* 48.12 (2023), pp. 4551–4571.

[10] Zonghua Pu et al. "Transition-metal phosphides: activity origin, energy-related electrocatalysis applications, and synthetic strategies". In: *Advanced Functional Materials* 30.45 (2020), p. 2004009.

[11] Qingwen Zhou et al. "Nitrogen-doped CoP electrocatalysts for coupled hydrogen evolution and sulfur generation with low energy consumption". In: *Advanced Materials* 30.27 (2018), p. 1800140.

[12] S Fujii, S Ishida, and S Asano. "Electronic structures and magnetic properties of Fe2P, Co2P and CoMnP". In: *Journal of Physics F: Metal Physics* 18.5 (1988), p. 971.

[13] Laifei Xiong et al. "Understanding the doping effect on hydrogen evolution activity of transition-metal phosphides: Modeled with Ni2P". In: *Applied Catalysis B: Environmental* 295 (2021), p. 120283.

[14] Robert B Wexler, John Mark P Martirez, and Andrew M Rappe. "Active role of phosphorus in the hydrogen evolving activity of nickel phosphide (0001) surfaces". In: *ACS Catalysis* 7.11 (2017), pp. 7718–7725.

[15] Yang Yang et al. "Insights into the origin of high activity of Ni5P4 (0001) for hydrogen evolution reaction". In: *The Journal of Physical Chemistry C* 127.11 (2023), pp. 5385–5394.

[16] Pengxia Ji et al. "Double metal diphosphide pair nanocages coupled with P-doped carbon for accelerated oxygen and hydrogen evolution kinetics". In: *ACS Applied Materials & Interfaces* 12.1 (2019), pp. 727–733.

[17] Wei Gao et al. "Modulating electronic structure of CoP electrocatalysts towards enhanced hydrogen evolution by Ce chemical doping in both acidic and basic media". In: *Nano energy* 38 (2017), pp. 290–296.

[18] Riyue Ge et al. "Hierarchical molybdenum phosphide coupled with carbon as a whole pH-range electrocatalyst for hydrogen evolution reaction". In: *Applied Catalysis B: Environmental* 260 (2020), p. 118196.

[19] Ping Liu and José A Rodriguez. "Catalysts for hydrogen evolution from the [NiFe] hydrogenase to the Ni2P (001) surface: the importance of ensemble effect". In: *Journal of the American Chemical Society* 127.42 (2005), pp. 14871–14878.

[20] Eric J Popczun et al. "Nanostructured nickel phosphide as an electrocatalyst for the hydrogen evolution reaction". In: *Journal of the American Chemical Society* 135.25 (2013), pp. 9267–9270.

[21] You Xu et al. "Anion-exchange synthesis of nanoporous FeP nanosheets as electrocatalysts for hydrogen evolution reaction". In: *Chemical Communications* 49.59 (2013), pp. 6656–6658.

[22] Jingqi Tian et al. "Self-supported nanoporous cobalt phosphide nanowire arrays: an efficient 3D hydrogen-evolving cathode over the wide range of pH 0–14". In: *Journal of the American Chemical Society* 136.21 (2014), pp. 7587–7590.

[23] Qian Liu et al. "Carbon nanotubes decorated with CoP nanocrystals: a highly active non-noble-metal nanohybrid electrocatalyst for hydrogen evolution". In: *Angewandte Chemie International Edition* 53.26 (2014), pp. 6710–6714.

[24] Zonghua Pu et al. "Tungsten phosphide nanorod arrays directly grown on carbon cloth: a highly efficient and stable hydrogen evolution cathode at all pH values". In: *ACS applied materials & interfaces* 6.24 (2014), pp. 21874–21879.

[25] Jingqi Tian et al. "Self-supported Cu3P nanowire arrays as an integrated high-performance three-dimensional cathode for generating hydrogen from water". In: *Angewandte Chemie* 126.36 (2014), pp. 9731–9735.

[26] Jakob Kibsgaard et al. "Designing an improved transition metal phosphide catalyst for hydrogen evolution using experimental and theoretical trends". In: *Energy & Environmental Science* 8.10 (2015), pp. 3022–3029.

[27] Anders B Laursen et al. "Climbing the volcano of electrocatalytic activity while avoiding catalyst corrosion: Ni3P, a hydrogen evolution electrocatalyst stable in both acid and alkali". In: *Acs Catalysis* 8.5 (2018), pp. 4408–4419.

[28] Sayan Banerjee et al. "Relationship between the surface reconstruction of nickel phosphides and their activity toward the hydrogen evolution reaction". In: *ACS Catalysis* 13.7 (2023), pp. 4611–4621.

[29] Sengeni Anantharaj et al. "Recent trends and perspectives in electrochemical water splitting with an emphasis on sulfide, selenide, and phosphide catalysts of Fe, Co, and Ni: a review". In: *Acs Catalysis* 6.12 (2016), pp. 8069–8097.

[30] Yuan Pan et al. "Monodispersed nickel phosphide nanocrystals with different phases: synthesis, characterization and electrocatalytic properties for hydrogen evolution". In: *Journal of Materials Chemistry A* 3.4 (2015), pp. 1656–1665.

[31] Shuang Cao et al. "Highly efficient photocatalytic hydrogen evolution by nickel phosphide nanoparticles from aqueous solution". In: *Chemical communications* 50.72 (2014), pp. 10427–10429.

[32] Ligang Feng et al. "Easily-prepared dinickel phosphide (Ni 2 P) nanoparticles as an efficient and robust electrocatalyst for hydrogen evolution". In: *Physical Chemistry Chemical Physics* 16.13 (2014), pp. 5917–5921.

[33] Hiroko Ariga et al. "Density function theoretical investigation on the Ni3PP structure and the hydrogen adsorption property of the Ni2P (0001) surface". In: *Chemistry letters* 42.12 (2013), pp. 1481–1483.

[34] Lauri Partanen, Mikko Hakala, and Kari Laasonen. "Hydrogen adsorption trends on various metal-doped Ni 2 P surfaces for optimal catalyst design". In: *Physical Chemistry Chemical Physics* 21.1 (2019), pp. 184–191.

[35] Qiuyi Yuan, Hiroko Ariga, and Kiyotaka Asakura. "An investigation of Ni 2 P single crystal surfaces: structure, electronic state and reactivity". In: *Topics in catalysis* 58 (2015), pp. 194–200.

[36] Ji-Sue Moon et al. "The nature of active sites of Ni2P electrocatalyst for hydrogen evolution reaction". In: *Journal of Catalysis* 326 (2015), pp. 92–99.

[37] Chen-Chen Weng, Jin-Tao Ren, and Zhong-Yong Yuan. "Transition metal phosphide-based materials for efficient electrochemical hydrogen evolution: a critical review". In: *ChemSusChem* 13.13 (2020), pp. 3357–3375.

[38] Martin H Hansen et al. "Widely available active sites on Ni 2 P for electrochemical hydrogen evolution–insights from first principles calculations". In: *Physical Chemistry Chemical Physics* 17.16 (2015), pp. 10823–10829.

[39] Zhongke Wang et al. "Water-Induced Formation of Ni2P–Ni12P5 Interfaces with Superior Electrocatalytic Activity toward Hydrogen Evolution Reaction". In: *Small* 17.6 (2021), p. 2006770.

[40] Caichi Liu et al. "Engineering Ni2P-NiSe2 heterostructure interface for highly efficient alkaline hydrogen evolution". In: *Applied Catalysis B: Environmental* 262 (2020), p. 118245.

[41] Linyuan Chen and Xian-Kui Wei. "A Review of the Structure–Property Relationship of Nickel Phosphides in Hydrogen Production". In: *Energies* 17.10 (2024), p. 2294.

[42] Sander Ø Hanslin, Hannes Jónsson, and Jaakko Akola. "Is the doped MoS 2 basal plane an efficient hydrogen evolution catalyst? Calculations of voltage-dependent activation energy". In: *Physical Chemistry Chemical Physics* 25.22 (2023), pp. 15162–15172.

[43] Alejandro J Garza, Alexis T Bell, and Martin Head-Gordon. "Mechanism of CO2 reduction at copper surfaces: pathways to C2 products". In: *Acs Catalysis* 8.2 (2018), pp. 1490–1499.

[44] Alejandro J Garza, Alexis T Bell, and Martin Head-Gordon. "Is subsurface oxygen necessary for the electrochemical reduction of CO2 on copper?" In: *The journal of physical chemistry letters* 9.3 (2018), pp. 601–606.

[45] Meenesh R Singh et al. "Mechanistic insights into electrochemical reduction of CO2 over Ag using density functional theory and transport models". In: *Proceedings of the National Academy of Sciences* 114.42 (2017), E8812–E8821.

[46] Fang Yu et al. "High-performance bifunctional porous non-noble metal phosphide catalyst for overall water splitting". In: *Nature communications* 9.1 (2018), p. 2551.

[47] Maxime Van den Bossche et al. "Assessment of constant-potential implicit solvation calculations of electrochemical energy barriers for H2 evolution on Pt". In: *The Journal of Physical Chemistry C* 123.7 (2019), pp. 4116–4124.

[48] Jason D Goodpaster, Alexis T Bell, and Martin Head-Gordon. "Identification of possible pathways for C–C bond formation during electrochemical reduction of CO2: new theoretical insights from an improved electrochemical model". In: *The journal of physical chemistry letters* 7.8 (2016), pp. 1471–1477.

[49] Yao Zheng et al. "The hydrogen evolution reaction in alkaline solution: from theory, single crystal models, to practical electrocatalysts". In: *Angewandte Chemie International Edition* 57.26 (2018), pp. 7568–7579.

[50] G. Kresse and J. Hafner. "Ab initio molecular-dynamics simulation of the liquid-metal–amorphous-semiconductor transition in germanium". In: *Phys. Rev. B* 49 (20 May 1994), pp. 14251–14269. DOI: 10.1103/PhysRevB.49.14251. URL: https://link.aps.org/doi/10.1103/PhysRevB.49.14251.

[51] G. Kresse and J. Furthmüller. "Efficiency of ab-initio total energy calculations for metals and semiconductors using a plane-wave basis set". In: *Computational Materials Science* 6.1 (1996), pp. 15–50. ISSN: 0927-0256. DOI: https://doi.org/10.1016/0927-0256(96)00008-0. URL: https://www.sciencedirect.com/science/article/pii/0927025696000080.

[52] G. Kresse and J. Furthmüller. "Efficient iterative schemes for ab initio total-energy calculations using a plane-wave basis set". In: *Phys. Rev. B* 54 (16 Oct. 1996), pp. 11169–11186. DOI: 10.1103/PhysRevB.54.11169. URL: https://link.aps.org/doi/10.1103/PhysRevB.54.11169.

[53] John P. Perdew, Kieron Burke, and Matthias Ernzerhof. "Generalized Gradient Approximation Made Simple". In: *Phys. Rev. Lett.* 77 (18 Oct. 1996), pp. 3865–3868. DOI: 10.1103/PhysRevLett.77.3865. URL: https://link.aps.org/doi/10.1103/PhysRevLett.77.3865.

[54] G. Kresse and D. Joubert. "From ultrasoft pseudopotentials to the projector augmented-wave method". In: *Phys. Rev. B* 59 (3 Jan. 1999), pp. 1758–1775. DOI: 10.1103/PhysRevB.59.1758. URL: https://link.aps.org/doi/10.1103/PhysRevB.59.1758.

[55] Stefan Grimme et al. "A consistent and accurate ab initio parametrization of density functional dispersion correction (DFT-D) for the 94 elements H-Pu". In: *The Journal of chemical physics* 132.15 (2010), p. 154104.

[56] Qunxiang Li and Xiao Hu. "First-principles study of Ni 2 P (0001) surfaces". In: *Physical Review B* 74.3 (2006), p. 035414.

[57] Robert B Wexler, John Mark P Martirez, and Andrew M Rappe. "Stable phosphorus-enriched (0001) surfaces of nickel phosphides". In: *Chemistry of Materials* 28.15 (2016), pp. 5365–5372.

[58] Junjie He et al. "The surface stability and equilibrium crystal morphology of Ni 2 P nanoparticles and nanowires from an ab initio atomistic thermodynamic approach". In: *CrystEngComm* 18.21 (2016), pp. 3808–3818.

[59] Jens Kehlet Nørskov et al. "Trends in the exchange current for hydrogen evolution". In: *Journal of The Electrochemical Society* 152.3 (2005), J23.

[60] JANAF Thermochemical Tables. *2d ed. Edited by DR Stull and H. Prophet No.* Tech. rep. NSRDS-NBS-37, US Government Printing Office, Washington, DC, 1971.

[61] Jeff Greeley et al. "Hydrogen evolution over bimetallic systems: Understanding the trends". In: *ChemPhysChem* 7.5 (2006), pp. 1032–1035.

[62] Mikko Hakala and Kari Laasonen. "Hydrogen adsorption trends on Al-doped Ni 2 P surfaces for optimal catalyst design". In: *Physical Chemistry Chemical Physics* 20.20 (2018), pp. 13785–13791.

[63] Karsten Reuter and Matthias Scheffler. "Composition, structure, and stability of RuO 2 (110) as a function of oxygen pressure". In: *Physical Review B* 65.3 (2001), p. 035406.

[64] Syam Sadan. *Adsorption Energy Data*. Dataset on Zenodo. Zenodo. June 2021. DOI: 10.5281/zenodo.12684848. URL: https://doi.org/10.5281/zenodo.12684848.

[65] Jing Zhu et al. "Recent advances in electrocatalytic hydrogen evolution using nanoparticles". In: *Chemical reviews* 120.2 (2019), pp. 851–918.

[66] K. Mathew, V. S. Chaitanya Kolluru, and R. G. Hennig. *VASPsol: Implicit solvation and electrolyte model for density-functional theory*. https://github.com/henniggroup/VASPsol. 2018. DOI: 10.5281/zenodo.2555053. URL: https://github.com/henniggroup/VASPsol.

[67] K. Mathew et al. “Implicit solvation model for density-functional study of nanocrystal surfaces and reaction pathways.” In: *J. Chem. Phys.* 140 (2014), p. 084106. DOI: 10.1063/1.4865107.

[68] K. Mathew et al. “Implicit self-consistent electrolyte model in plane-wave density-functional theory.” In: *J. Chem. Phys.* 151 (2019), p. 234101. DOI: 10.1063/1.5132354.

[69] SA Petrosyan et al. “Joint density-functional theory for electronic structure of solvated systems”. In: *Physical Review B* 75.20 (2007), p. 205105.

[70] Hannes Jónsson, Greg Mills, and Karsten W Jacobsen. “Nudged elastic band method for finding minimum energy paths of transitions”. In: *Classical and quantum dynamics in condensed phase simulations*. World Scientific, 1998, pp. 385–404.

[71] Graeme Henkelman and Hannes Jónsson. “Improved tangent estimate in the nudged elastic band method for finding minimum energy paths and saddle points”. In: *The Journal of chemical physics* 113.22 (2000), pp. 9978–9985.

[72] Graeme Henkelman, Blas P Uberuaga, and Hannes Jónsson. “A climbing image nudged elastic band method for finding saddle points and minimum energy paths”. In: *The Journal of chemical physics* 113.22 (2000), pp. 9901–9904.

[73] Erik Bitzek et al. “Structural relaxation made simple”. In: *Physical review letters* 97.17 (2006), p. 170201.

[74] Daniel Sheppard, Rye Terrell, and Graeme Henkelman. “Optimization methods for finding minimum energy paths”. In: *The Journal of chemical physics* 128.13 (2008), p. 134106.

[75] Syam Sadan. *HER energy profile, CI-Nudged Elastic Band calculations*. Dataset on Zenodo. 2023. DOI: 10.5281/zenodo.12685655. URL: https://doi.org/10.5281/zenodo.12685655.

[76] Stig Rundqvist. “X-Ray Investigations of Mn, P., Mn, P, and Ni, P”. In: *Acta Chemica Scandinavica* 4 (1962), p. 992.

[77] Shrinath Dattatray Ghadge et al. “Computational and experimental investigation of Co and S-doped Ni 2 P as an efficient electrocatalyst for acid mediated proton exchange membrane hydrogen evolution reaction”. In: *Catalysis Science & Technology* 11.3 (2021), pp. 861–873.

[78] Shushi Suzuki et al. “Scanning tunneling microscopy and photoemission electron microscopy studies on single crystal Ni2P surfaces”. In: *Journal of nanoscience and nanotechnology* 9.1 (2009), pp. 195–201.

[79] Md Golam Moula et al. “The first atomic-scale observation of a Ni2P (0001) single crystal surface”. In: *Chemistry letters* 35.1 (2006), pp. 90–91.

[80] Lihuang Jin et al. “Phase separation synthesis of trinickel monophosphide porous hollow nanospheres for efficient hydrogen evolution”. In: *Journal of Materials Chemistry A* 4.28 (2016), pp. 10925–10932.

[81] Donghui Guo et al. “STM studies on the reconstruction of the Ni2P (1010) surface”. In: *Surface science* 604.17-18 (2010), pp. 1347–1352.

[82] Alvin B Hernandez et al. “Dynamical LEED analysis of Ni2P (0 0 0 1)-1× 1: Evidence for P-covered surface structure”. In: *Chemical Physics Letters* 513.1-3 (2011), pp. 48–52.

[83] Ping Liu et al. “Desulfurization reactions on Ni2P (001) and α-Mo2C (001) surfaces: complex role of P and C sites”. In: *The Journal of Physical Chemistry B* 109.10 (2005), pp. 4575–4583.

[84] Alba B Vidal et al. “Unraveling the Structure and Surface Chemistry of the Phosphosulfide Phase Formed on Ni2P under Hydrodesulfurization Reaction Conditions: A DFT Study”. In: *The Journal of Physical Chemistry C* 126.33 (2022), pp. 14187–14200.

[85] Jiawei Zhang, Peijun Hu, and Haifeng Wang. “Amorphous catalysis: machine learning driven high-throughput screening of superior active site for hydrogen evolution reaction”. In: *The Journal of Physical Chemistry C* 124.19 (2020), pp. 10483–10494.